Available online at www.sciencedirect.com

ScienceDirect

Procedia Manufacturing 34 (2019) 73–82

Procedia MANUFACTURING

www.elsevier.com/locate/procedia

47th SME North American Manufacturing Research Conference, Penn State Behrend Erie, Pennsylvania, 2019

The sliding friction contact frequency response function

Christoph Kossack, John Ziegert, and Tony Schmitz*

University of North Carolina at Charlotte, Charlotte, NC, 28223, USA

* Corresponding author. Tel.: +1-704-687-5086; fax: +1-704-687-8345. *E-mail address:* tony.schmitz@uncc.edu

Abstract

This paper details frequency response function (FRF) measurement and simulation for a dynamic oscillator with a sliding (Coulomb) friction contact. The oscillator is approximated physically using the friction measuring machine (FMM), a parallelogram leaf-type flexure with a sliding friction contact. The flexure-based FMM provides linear motion between a polytetrafluouroethylene pin and (lubricated) polished steel counterface. Both the input force and response velocity are measured by impact testing to determine the FRF. Numerical simulations are completed to identify the best-fit friction coefficient for three input force levels (450 N, 1000 N, and 1450 N). It is shown that: 1) the FRF magnitude increases linearly with impulse (i.e., the area under the time domain force profile); and 2) a single friction coefficient (0.113) is sufficient to describe the dynamic response for the three force levels.

Keywords: Friction; Coulomb; dynamics; transient; impact testing

1. Introduction

In the study of dynamic systems, the frequency response function, or FRF, is a powerful analytical and experimental analysis tool. It defines the complex-valued frequency domain behavior, typically represented as the magnitude and phase or, alternately, the real and imaginary parts versus excitation frequency [1]. Modal testing provides a common experimental approach for identifying structural dynamics in the form of the FRF [2]. The application of impact testing, where an instrumented hammer is used to excite the structure over a sufficient bandwidth and a linear transducer is used to measure the corresponding vibratory response, is widespread in both industry and academia. While impact testing for flexible structures is commonplace, its use for measuring the dynamic response of systems with sliding contact is largely unexplored.

In this paper, an experimental platform (the friction measuring machine, or FMM) is described that enables transient, linear sliding motion between friction contact pairs under constant normal force loading [3-4]. Using the FMM, impact tests are completed with a hammer and laser vibrometer. The hammer provides the input energy in the form of a short duration impact and the system oscillates until it comes to rest (typically not at its starting position). The vibrometer measures the velocity during the decaying response as energy is dissipated in the friction contact. These experimental results are combined with simulation in order to parameterize idealized dynamic models that include friction.

The paper is organized as follows. First, preliminary background information on friction is provided. Second, a dynamic oscillator with sliding (Coulomb) friction is used to model sliding contacts and the second order differential equation of motion is defined [5]. Time domain solution of the equation of motion is then completed and example results are presented, including: the variation in final position with initial position for free vibration; and the FRF for an impulsive force input. Third, the flexure-based FMM is described [3-4]. Fourth, experimental results are presented and compared to numerical simulation. Finally, conclusions are presented.

10.1016/j.promfg.2019.06.119

2. Background

Friction, which can be defined as the resistance to relative sliding between two bodies in contact under a normal load [6], is ubiquitous in manufacturing, metrology, mechanical design, and control. For manufacturing processes such as forging, rolling, extrusion, drawing, sheet metal forming, machining, and grinding, friction tends to increase the required force and power; therefore, the associated cost is significant. In forging, for example, friction forces at the die-workpiece interface can cause barreling, which yields inhomogeneous deformation patterns within the workpiece. It also leads to the familiar "friction hill" pressure distribution at the die-workpiece interface. In metal cutting, a high friction force is developed between the sheared chip and the rake face of the cutting tool in the secondary shear zone [6-10]. This, in turn, generates heat which tends to increase tool wear rates. For these and other reasons, the synthesis and testing of new lubricants and coatings to be used in manufacturing processes is an important, and continuous, research objective. Friction is also a necessary phenomenon, however. Without it, rolling, or reducing workpiece thickness using compressive forces applied by opposing rolls, would not be possible because the workpiece would not be pulled into the gap between the rolls.

Friction must also be considered in the control of manufacturing and metrology equipment. Servo-controlled, multi-axis positioning systems are widely used in: conventional and ultra-high precision machine tools; coordinate measuring machines; semi-conductor lithography equipment; micro- and nano-manufacturing systems; satellite imaging systems; and others. In many applications, axis positioning accuracies on the order of one part in 10^6 (or less) of the range of motion is required. For these high accuracy applications, motion velocities and accelerations are typically small, with the result that friction is often the dominant force in the system. This is true even when efforts are made to use very low friction interfaces, such as hydrostatic, aerostatic, or rolling contact bearings. Despite the use of tribological elements designed to reduce friction, it can still play a significant role in the system's positioning repeatability and accuracy [11].

Numerous strategies to account for and compensate frictional effects in position control systems have been reported [e.g, 11-15]. However, implementation of model-based control is challenging because simple Coulomb-type friction models and many more advanced models, such as the Dahl, LuGre, Leuven, and generalized Maxwell-slip models, are discontinuous or piecewise continuous [16-25]. This poses a challenge for high performance continuous controllers (e.g., sliding mode control). Makkar *et al*. [26] presented a continuous and differentiable friction model which accounts for static and low-speed effects, position dependence, asymmetries, the Stribeck effect, and viscous damping. Other models are also available.

One common feature of these friction models is characterization of the frictional response near zero sliding speeds, where the "stiction" behavior transitions from no-slip to sliding motion. This is also the most critical region for high precision positioning controllers, particularly at motion reversals [27]. For example, cameras used for satellite imagery are positioned in low earth orbit at heights ranging from 300 km to 2000 km. In order for the camera to move its image point by 10 m on the earth's surface, the controller must be able to rotate the camera between 0.002 deg and 0.0003 deg, depending on the satellite height. Accurate realization of such motion is dependent on accurate characterization of the frictional behavior of the system near zero velocity.

Due to these considerations, modeling and measurement of friction behavior is a critical research topic for both engineering and the physical sciences. Friction models, such as those based on adhesion or other mechanisms, relate surface condition, normal load, sliding velocity, temperature, and environment, for example, to friction forces. Traditional friction measurement attempts to assign known operating conditions, while recording the resulting friction forces. In this way, friction models may be validated (or modified) and the performance of new lubricants and coatings may be assessed. In this research, this traditional force-based (Newtonian) friction measurement paradigm is replaced by a displacement-based (Lagrangian) strategy. In prior work, the measurement uncertainty for the force-based approach was evaluated and it was determined that its accuracy, particularly at low friction conditions, is limited [28]. This motivates the alternate Lagrangian measurement technique implemented here.

3. Sliding contact model

In this work the dynamic oscillator displayed in Fig. 1 is used to model sliding friction. When the mass is given an initial displacement from its equilibrium position, for example, this displacement characterizes the initial energy input to the system. The system is then released and allowed to oscillate (for sufficiently low friction) until motion ceases. If the final rest position differs from the equilibrium position, energy remains in the system. During the decaying oscillation, the time dependent displacement and velocity describe the transient response. This characterizes the energy dissipation in a continuous time record. The dissipation describes the friction behavior at the interface over a range of sliding velocities from near-zero to the maximum. Alternately, the input energy can be imposed in the form of an impulsive force. Again, the system oscillates until the motion stops due to frictional energy loss.

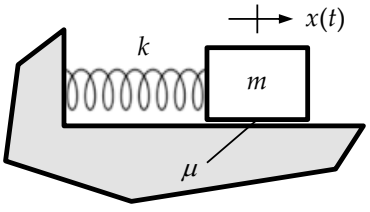

Figure 1: Spring-mass oscillator with Coulomb friction.

Sliding, or Coulomb, friction is incorporated into the single degree of freedom, free vibration equation of motion that describes the time dependent displacement, $x(t)$, of the Fig. 1 spring-mass system as shown in Eq. 1. In this equation, the time dependence is implied, m is the mass, k is the linear spring constant, and F_f is the friction force. For the Coulomb model,

the friction force is equal to the product of the friction coefficient, μ, and the normal force, $N = mg$.

$$\begin{aligned} m\ddot{x} + kx + F_f &= 0, \dot{x} > 0 \\ m\ddot{x} + kx &= 0, \dot{x} = 0 \\ m\ddot{x} + kx - F_f &= 0, \dot{x} < 0 \end{aligned} \quad (1)$$

Because the friction force always opposes the velocity direction, it is discontinuous. This yields the nonlinear second order, homogeneous differential equation shown in Eq. 1 [5]. For the displacement-based approach adopted in this research, the desired information is $x(t)$ or, similarly, velocity, $\dot{x}(t)$. While this paper's focus is FRF measurement and friction model parameterization, an interesting exercise for the solution of Eq. 1 is to establish the relationship between the initial mass displacement, $x(0) = x_0$, and the corresponding motion. Specifically, due to the friction force, the final displacement, x_f, depends on x_0.

To demonstrate, consider the low friction case where μ = 0.1, m = 1 kg, and k = 5×10^3 N/m for the model in Fig. 1. The free vibration response for x_0 = 3 mm (zero initial velocity) is displayed in Fig. 2, where x_f = -0.139 mm. It is observed that when the velocity reaches zero, if the current displacement is between $x_{lim} = \frac{F_f}{k} = \frac{\mu N}{k}$ and $-x_{lim}$, the motion stops. This limiting displacement (marked by the horizontal dashed lines in the top panel of Fig. 2) is the x value where the spring force is equal to or less than the maximum friction force. For a new initial displacement of $x_0 = 1$ mm, the final mass position is x_f = 0.176 mm; see Fig. 3. The results in Figs. 2 and 3 were obtained by fixed time step numerical integration of Eq. 1, where the acceleration is calculated at each time step and the corresponding velocity and displacement are determined by Euler integration. The time step was selected to be 1×10^4 times smaller than the oscillating period for numerical accuracy.

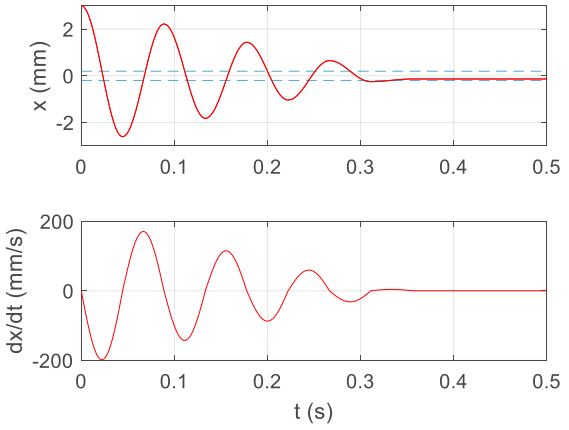

Figure 2: Free vibration result for x_0 = 3 mm (zero initial velocity). (Top) Mass displacement versus time. (Bottom) Mass velocity versus time.

If the final displacement is plotted versus the initial displacement for the Fig. 1 system, a periodic structure is revealed. This result is presented in Fig. 4, where the numerical simulation was repeated for initial displacements from 0 to 5 mm in steps of 0.005 mm (horizontal axis) and the final displacement was recorded for each iteration (vertical axis). The period of the triangular waveform is $\frac{4F_f}{k} = \frac{4\mu N}{k}$ and its magnitude is x_{lim}.

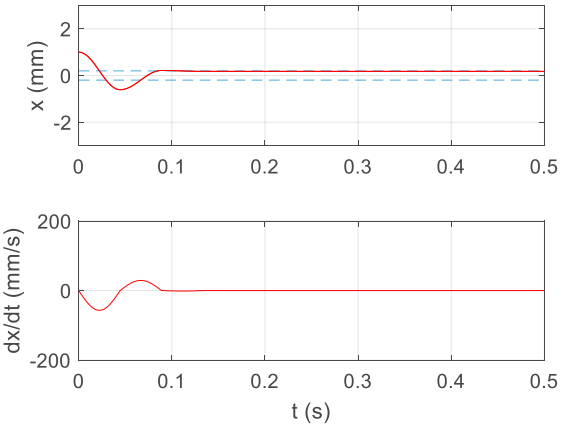

Figure 3: Free vibration result for x_0 = 1 mm (zero initial velocity). (Top) Mass displacement versus time. (Bottom) Mass velocity versus time.

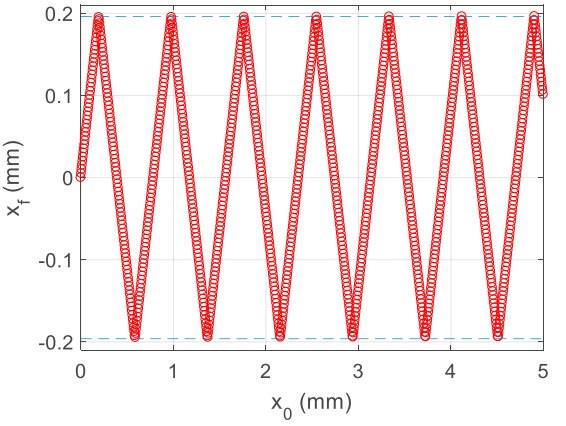

Figure 4: Initial versus final displacement for free vibration of the dynamic oscillator with Coulomb friction.

The numerical simulation was next modified to include an impulsive force input, rather than an initial displacement, to initiate the oscillatory motion. The new differential equation of motion is provided in Eq. 2, where f is the impulsive force input. Given the time domain force input and corresponding response output (displacement or velocity), the FRF is determined by calculating:

1. the discrete Fourier transform of the time domain force input to convert to the frequency domain
2. the discrete Fourier transform of the time domain displacement or velocity output
3. their complex-valued, frequency domain ratio.

If displacement is selected, the receptance FRF, $\frac{X}{F}(\omega)$, is obtained, where ω is the excitation frequency in rad/s. For

velocity, the mobility FRF, $\frac{V}{F}(\omega)$, is obtained, where V is the complex-valued velocity in the frequency domain.

$$\begin{aligned} m\ddot{x} + kx + F_f &= f, \dot{x} > 0 \\ m\ddot{x} + kx &= f, \dot{x} = 0 \\ m\ddot{x} + kx - F_f &= f, \dot{x} < 0 \end{aligned} \quad (2)$$

The numerical simulation was modified to include a rectangular force input with a short duration, Δt; its magnitude was constant over Δt and zero otherwise. The time domain input force and output displacement signals are presented in Fig. 5 for three Δt values: {2.5, 5, and 10} ms. Note the linear decay in the oscillating displacement peaks. This is indicative of friction energy dissipation and contrary to the exponential decay observed for viscous damping [5]. The corresponding frequency domain signals are displayed in Fig. 6. The receptance FRFs are shown in Fig. 7. Note that a total sampling time of 25 s was selected to provide adequate frequency resolution. These results demonstrate that the response changes with the amount of energy input into the system (i.e., the area under the force curve).

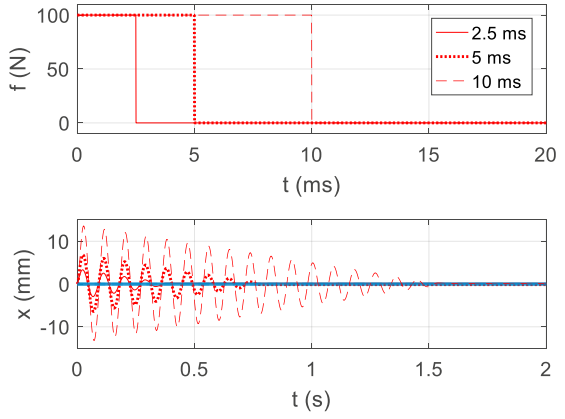

Figure 5: (Top) Impulse force input for three Δt values; (bottom) displacement output. Note the change in range for the time axes between the top and bottom panels.

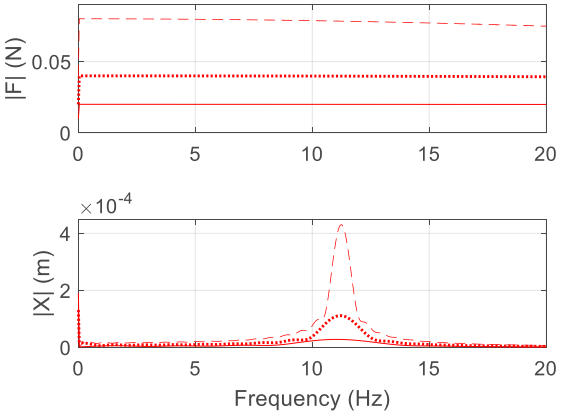

Figure 6: (Top) Input force magnitude versus frequency for three Δt values (same legend as Fig. 5). (Bottom) Output displacement magnitude versus frequency. The response peaks are observed at the dynamic oscillator's undamped natural frequency of $f_n = \frac{1}{2\pi}\sqrt{\frac{k}{m}} = 11.25$ Hz.

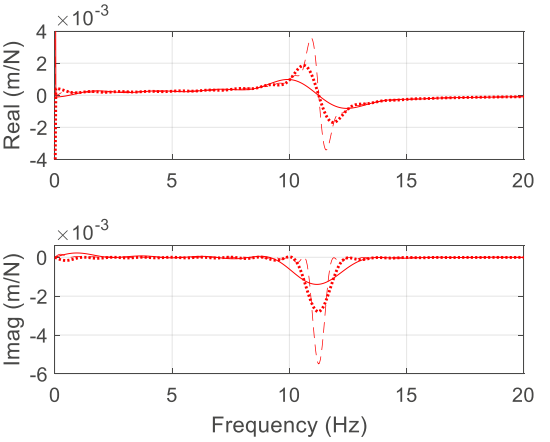

Figure 7: (Top) Real part of the receptance FRF for three Δt values (same legend as Fig. 5). (Bottom) Imaginary part of the receptance FRF.

For comparison purposes, a constant duration of Δt = 10 ms was selected and the force magnitude was varied: {25, 50, and 100} N. These three cases provided the same impulse (i.e., area under the time domain force profile), {0.25, 0.5, and 1} N-s, as the three previous cases shown in Figs. 5-7. Identical FRFs were obtained, but are not shown for brevity.

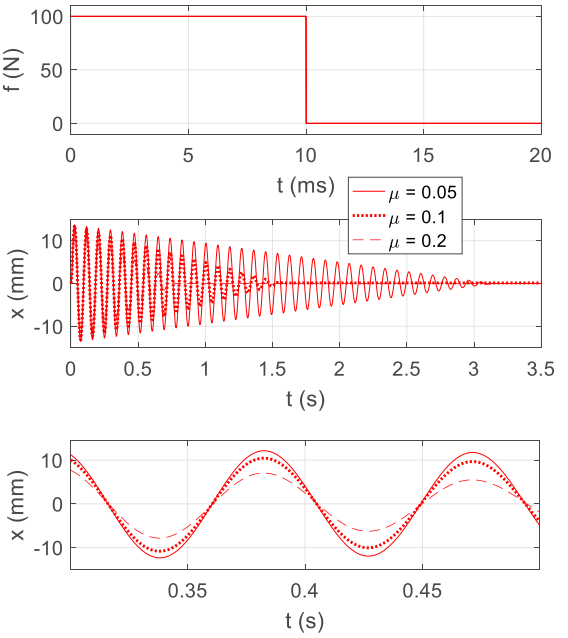

Figure 8: (Top) Impulse force input. (Middle) Displacement output for three friction coefficient values. (Bottom) Three displacement signals for the initial part of the motion. Because there was a separate x_{lim} value for each friction coefficient, these lines were not included in the plot. Note the change in range for the time axes between the top and middle panels.

In addition to the impulse value, changes in the friction force magnitude also modify the system response. In a second numerical study, F_f in Eqs. 1 and 2 was varied for a constant impulsive force input (Δt = 10 ms with a magnitude of 100 N). In the Fig. 1 model, the normal force is fixed by the mass so the friction force can only be changed by increasing or decreasing the friction coefficient. In the experimental setup used in this research (i.e., the FMM), the normal force was set independently so this restriction was avoided. For the purposes of this numerical examination, however, the mass was kept constant and three friction coefficients were selected: μ = 0.05, 0.1, and 0.2. These results are displayed in Figs. 8-10.

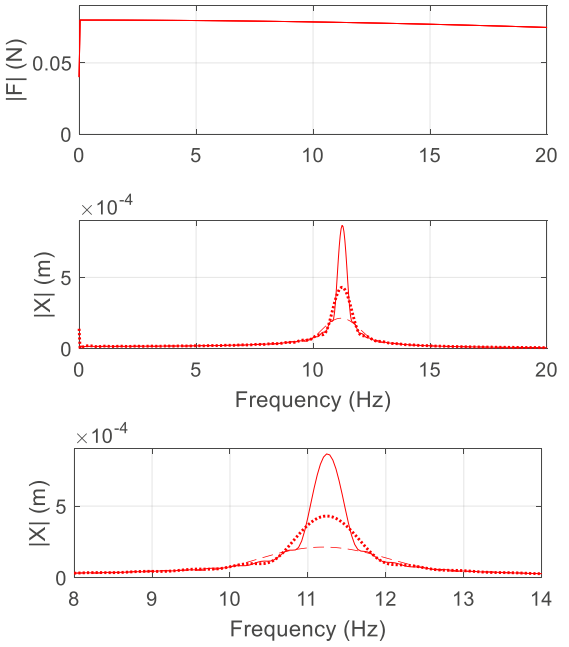

Figure 9: (Top) Input force magnitude versus frequency. (Middle) Output displacement magnitude for three friction coefficient values (same legend as Fig. 8). (Bottom) Magnified view of the displacement magnitude near the natural frequency.

4. Experimental setup

The FMM provides relative linear motion between a friction contact pair (pin and flat counterface) using a parallelogram, leaf-type flexure. Figure 11 displays the four leaf spring arrangement, where one end of each spring is clamped to a rigid base and the other is clamped to a faceplate which carries the motion platform. An electromagnet (not shown) is used to provide an initial displacement, when required. For the purposes of this study, however, the input energy was supplied by the hammer impact which was applied to the motion platform at the middle of the leaf spring length to minimize platform rotation. A capacitance sensor (not shown) was used to monitor parasitic motion (i.e., arc motion perpendicular to the desired motion direction) of the platform. It was negligible when compared to the linear motion magnitude (e.g., 30 µm maximum parasitic motion for a 6 mm platform displacement).

The FMM dynamics with no friction contact were determined by: 1) imposing an initial displacement to the motion platform with the electromagnet (not shown in Fig. 11); 2) measuring the corresponding free vibration velocity after release; and 3) using a nonlinear least squares optimization function in MATLAB (lsqnonlin) to solve for the mass, damping, and spring constants that minimized the difference between the measured velocity and the solution to the damped oscillator's second order differential equation of motion, $m\ddot{x} + c\dot{x} + kx = 0$, where c is the viscous damping constant that was included to account for the small energy dissipation during the flexure motion. The results were: m = 10.391 kg, c = 0.275 N-s/m, and k = 1982 N/m. The corresponding undamped natural frequency and viscous damping ratio were: $f_n = \frac{1}{2\pi}\sqrt{\frac{1982}{10.391}} = 2.20$ Hz and $\zeta = \frac{c}{2\sqrt{km}} = \frac{0.275}{2\sqrt{1982(10.391)}} = 0.00096 = 0.096\%$. Fixed time step numerical integration was used to solve the equation of motion and determine the model parameters, rather than impact testing and modal fitting, because the damping was so low.

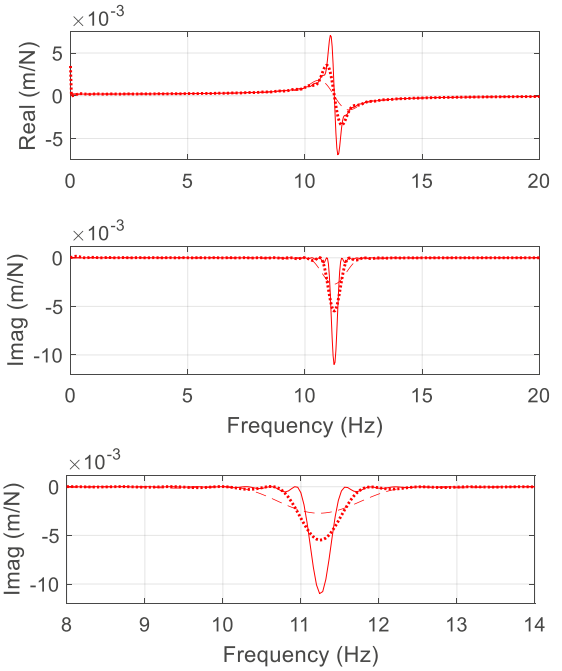

Figure 10: (Top) Real part of the receptance FRF for three friction coefficient values (same legend as Fig. 8). (Middle) Imaginary part of the receptance FRF. (Bottom) Magnified view of the imaginary part of the FRF near the natural frequency.

The FMM friction contact for FRF testing is produced between the pin and counterface. The pin is clamped into a holder and then attached to the vertical shaft shown in Fig. 11. The shaft is supported by a pair of air bearings, which are rigidly attached to the base. The normal force between the pin and counterface is provided by a mass attached to the top of the vertical shaft. The mass for the tests completed in this study was 0.680 kg (normal force of 6.67 N).

After the pin is clamped to the vertical shaft, it is lowered onto sandpaper which is attached by adhesive tape to the counterface. The sample is then moved back and forth for several interations to ensure that the contacting surfaces are flat and parallel. This is repeated for a range of increasing grit numbers to leave a smooth pin face. For the tests performed here, the contact pair consisted of a polytetrafluouroethylene (PTFE) pin on a polished steel counterface. The interface was lubricated using CRC Ultra Lite 3-36 Ultra Thin Non Staining Lubricant. The lubrication was applied to ensure that each impact force level selected for testing would result in a sufficient number of oscillations during the decaying motion.

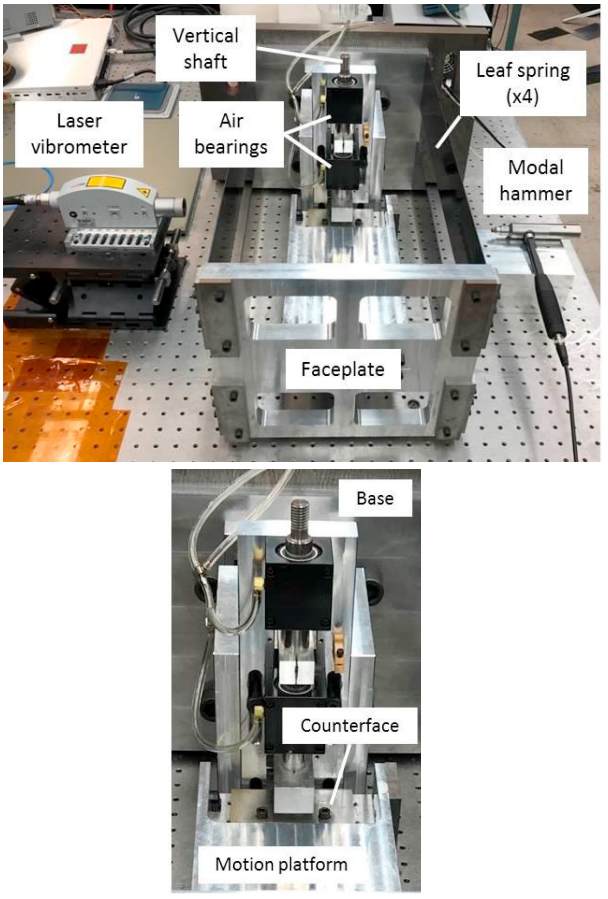

Figure 11: Photographs of FMM. They key components are identified.

Three impact force ranges were applied to the FMM using the impact hammer. Since the impact hammer is a manual device and repeating the same force level with each impact is not possible, a tolerance of ±50 N was selected for impact acceptance. The nominal impact force levels were 450 N (low), 1000 N (medium), and 1450 N (high). The impact force was applied using a PCB 086D05 modally tuned hammer with added mass and a rubber tip. The corresponding velocity was measured using a Polytec OFV-534 laser vibrometer head and OFV-5000 controller. The sampling time for each test was selected to be 33 s to ensure adequate frequency resolution for the FRFs. The sampling frequency was 10 kHz. The FMM was impacted by the hammer 10 times for each nominal force level. Between each impact, the CRC Ultra Lite 3-36 was reapplied to the counterface to ensure a consistent lubrication condition.

5. Results

The measured time domain force and velocity signals were imported into MATLAB for analysis. Figure 12 displays the impact force and velocity data for 10 trials at the medium impact level.

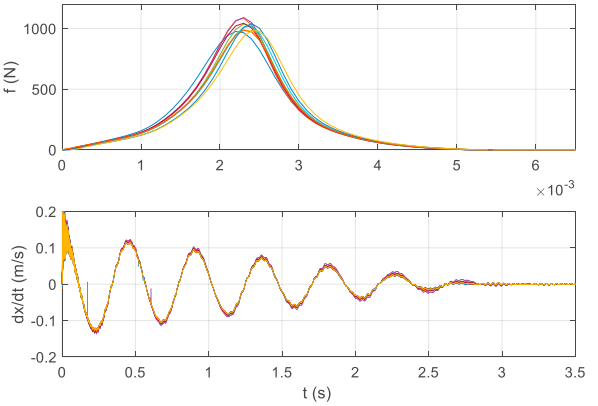

Figure 12: (Top) Time domain force, f, for 1000 N (medium) level. (Bottom) Time domain velocity, $\dot{x}$, due to force input. Note the change in time scale between the top and bottom panels.

For each of the three force levels, the impulse was calculated (i.e., the area under the time domain force profile). It was determined using the trapezoid rule with a step size of 1×10^{-4} s (i.e., the sampling period). Figure 13 displays the results. For the right panel, the mean impulse value at each force level is shown with an error bar that represents ±1 standard deviation over the 10 trials.

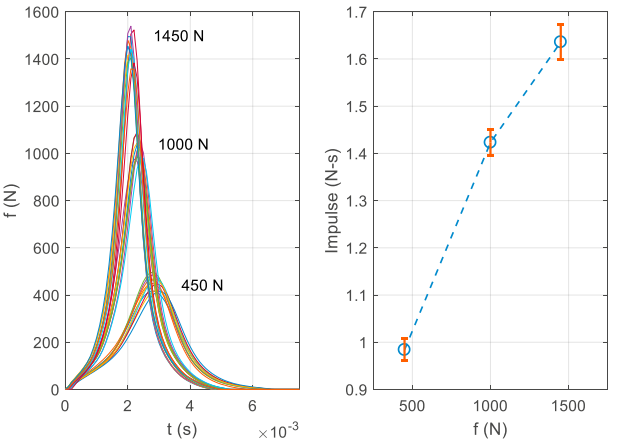

Figure 13: (Left) Three impact force levels. (Right) Impulse values for the three force levels.

The FRFs for the three force levels were determined by converting the time domain force and velocity signals into the frequency domain using the discrete Fourier transform. The

mobility for each data set was then calculated by dividing the frequency domain velocity by the frequency domain force. Figure 14 displays the real and imaginary parts of the mobility for 10 trials at the medium force level. To convert to receptance, the mobility FRF was divided by $i\omega$. This follows from an assumption of harmonic motion, where $x = Xe^{i\omega t}$ and $\dot{x} = i\omega Xe^{i\omega t}$. The corresponding receptance is shown in Fig. 15.

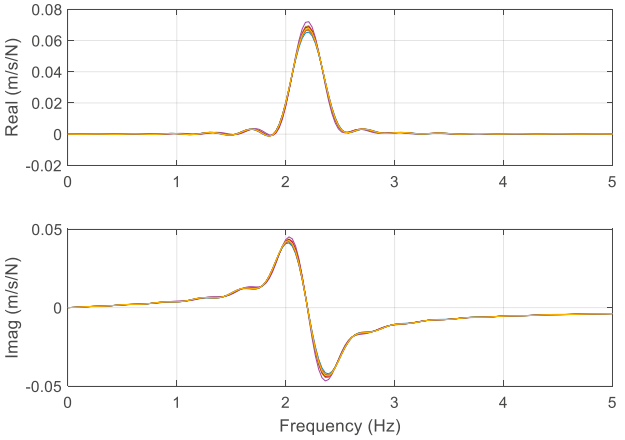

Figure 14: (Top) Real part of mobility FRF for 10 trials at the 1000 N (medium) force level. (Bottom) Imaginary part of mobility FRF for 10 trials.

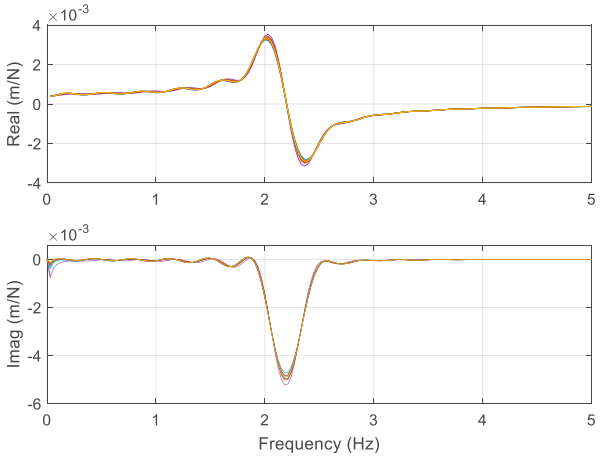

Figure 15: (Top) Real part of receptance FRF for 10 trials at the 1000 N (medium) force level. (Bottom) Imaginary part of receptance FRF for 10 trials.

The receptances are next compared for the three force levels. Figure 16 displays the mean FRF magnitudes for the low, medium, and high levels (10 trials each, averaged in the frequency domain). Figure 17 shows the impulse versus receptance magnitude for the three force levels (mean impulse values of 0.98 N-s, 1.42 N-s and 1.64 N-s), where the + symbol identifies the mean of 10 trials at each level. A linear trend is observed with an R^2 value very close to unity.

Next, Eq. 2 was modified to include both sliding friction and viscous damping as shown in Eq. 3 [29]. Equation 3 was solved by fixed time step numerical integration and the friction coefficient was identified to provide a best fit to the measured mobility FRFs. The measured force from the impact hammer, f, was used as input to Eq. 3 to avoid introducing errors due to approximations of the excitation force. Because the sampling frequency for the measured force was 10 kHz, the numerical integration time step was 1×10^{-4} s.

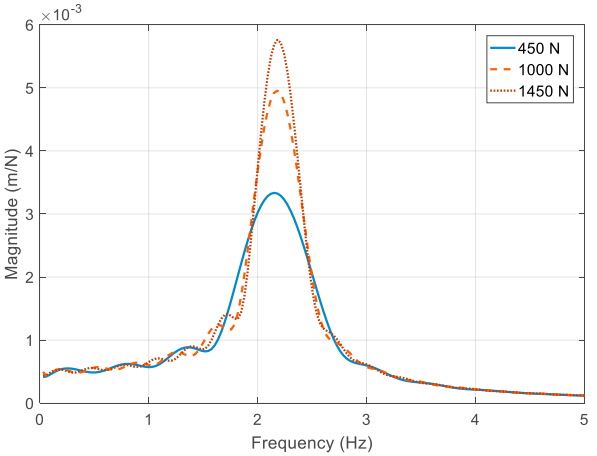

Figure 16: Mean receptance magnitude at three force levels. The magnitude increases with force for the FMM with friction contact.

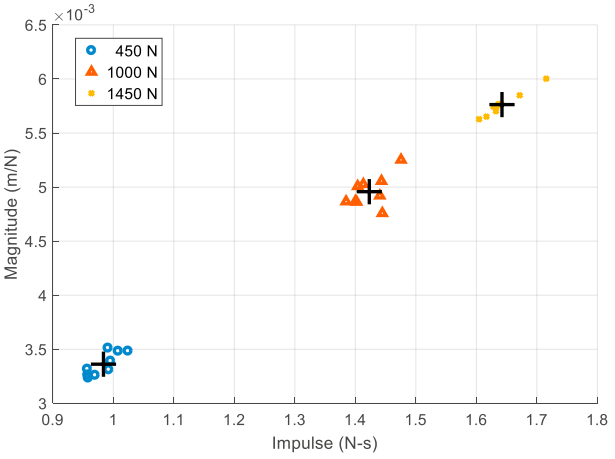

Figure 17: Impulse versus receptance magnitude for the three force levels.

$$\begin{aligned} m\ddot{x} + c\dot{x} + kx + F_f &= f, \dot{x} > 0 \\ m\ddot{x} + c\dot{x} + kx &= f, \dot{x} = 0 \\ m\ddot{x} + c\dot{x} + kx - F_f &= f, \dot{x} < 0 \end{aligned} \tag{3}$$

A result for the 450 N (low) force level is shown in Fig. 18. The measured force is displayed in the top panel, while the simulated (solid line) and measured (dotted line) velocity are displayed in the bottom panel. The friction coefficient is 0.113. Figure 19 shows the corresponding mobility FRF. The 1000 N (medium) force levels results are provided in Figs. 20 and 21. The 1450 N (high) force level results are shown in Figs. 22 and 23. The friction coefficient is 0.113 in all cases.

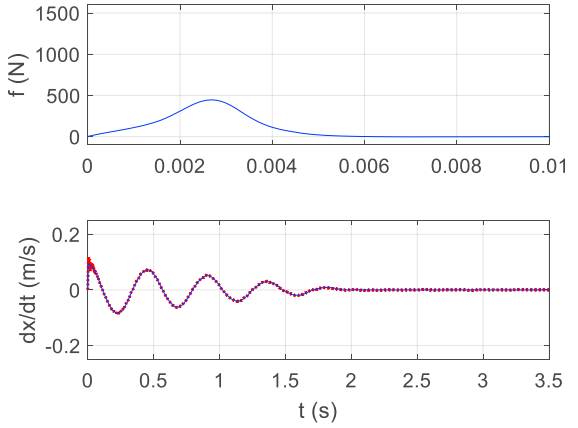

Figure 18: (Top) Low force level (450 N) input. (Bottom) Simulated (solid) and measured (dotted) velocity for 0.113 friction coefficient. Note that the top and bottom panels have different time scales.

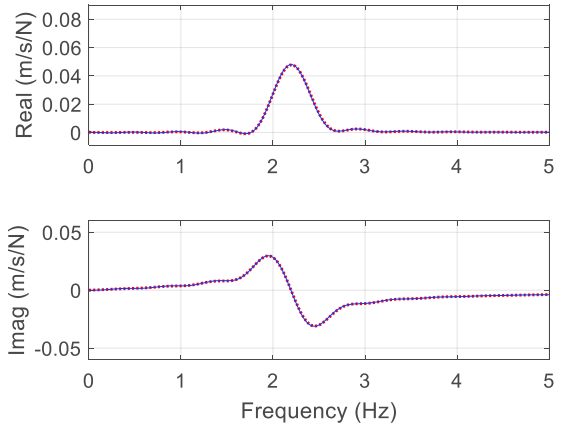

Figure 19: (Top) Real part of simulated (solid) and measured (dotted) mobility FRF for the low (450 N) force level with a friction coefficient of 0.113. (Bottom) Imaginary part of simulated and measured mobility FRFs.

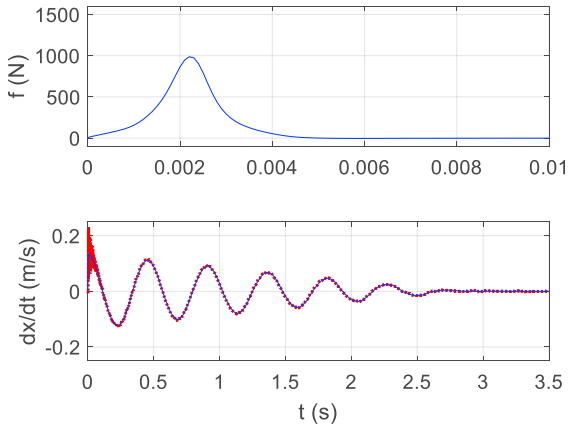

Figure 20: (Top) Medium force level (1000 N) input. (Bottom) Simulated (solid) and measured (dotted) velocity for 0.113 friction coefficient. Note that the top and bottom panels have different time scales.

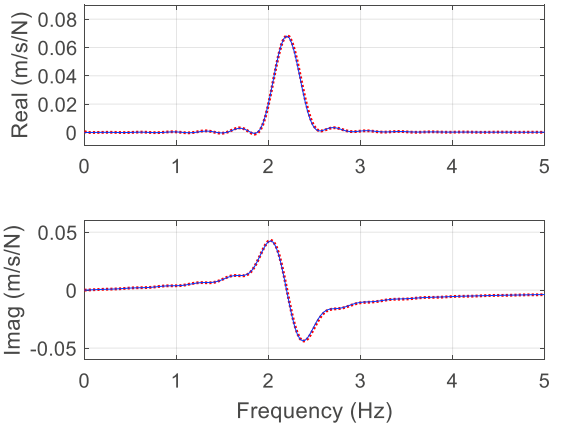

Figure 21: (Top) Real part of simulated (solid) and measured (dotted) mobility FRF for the medium (1000 N) force level with a friction coefficient of 0.113. (Bottom) Imaginary part of simulated and measured mobility FRFs.

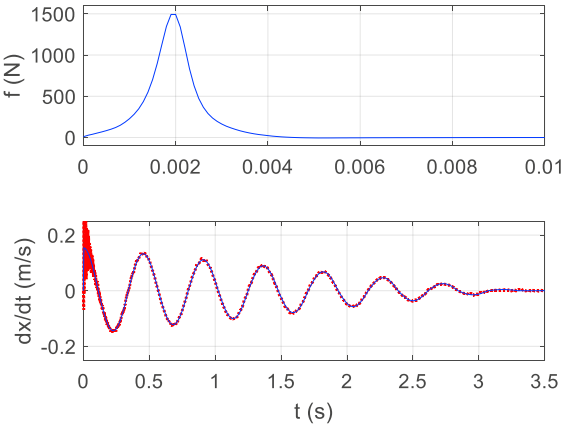

Figure 22: (Top) High force level (1450 N) input. (Bottom) Simulated (solid) and measured (dotted) velocity for 0.113 friction coefficient. Note that the top and bottom panels have different time scales.

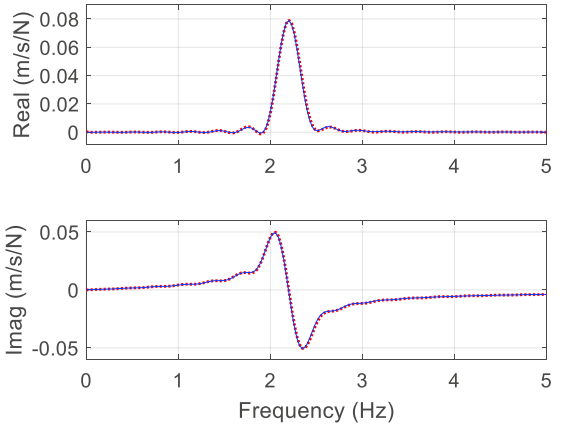

Figure 23: (Top) Real part of simulated (solid) and measured (dotted) mobility FRF for the high (1450 N) force level with a friction coefficient of 0.113. (Bottom) Imaginary part of simulated and measured mobility FRFs.

The frequency range for the medium force level result is extended to 20 Hz in Fig. 24. Interestingly, it is seen that odd multiples (3, 5, 7, 9, …) of the 2.2 Hz natural frequency appear in both the simulated and measured mobility FRFs. This result was observed at all three force levels. Since the numerical model included only the single degree of freedom dynamics, this must be a sliding friction phenomenon, rather than the influence of other vibration modes in the FMM structure.

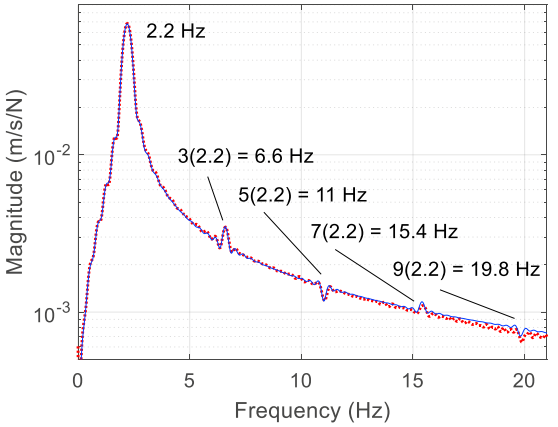

Figure 24: Logarithmic magnitude of simulated (solid) and measured (dotted) mobility FRF for the medium (1000 N) force level with a friction coefficient of 0.113.

6. Conclusions

This paper described frequency response function (FRF) measurement and simulation for a damped oscillator with a sliding (Coulomb) friction contact. The dynamic system was realized using the parallelogram leaf-type flexure-based friction measuring machine (FMM). The FMM enabled linear motion between a pin-counterface friction contact with impact force input. The corresponding velocity was measured to characterize the energy dissipation. Results were presented for a lubricated polytetrafluouroethylene-polished steel contact. It was observed that the FRF magnitude increased linearly with impulse (i.e., the area under the time domain force profile), which is indicative of the nonlinear friction behavior (and model). It was also seen that a single friction coefficient was sufficient to describe the response under three force levels (450 N, 1000 N, and 1450 N).

This approach is most applicable to dynamics systems where friction energy dissipation cannot be neglected and it is not effectively modeled by an equivalent viscous damping approach. This could include a positioning axis, for example, where the dynamic response must be included in a closed-loop control algorithm. Because friction can dominate when velocities and displacements are low, closed-loop position control is particularly relevant. Using the impact testing experimental approach presented here, the structural dynamics model can described as shown in Eq. 3 and the model parameters can be identified.

Acknowledgements

The authors acknowledge the contributions of C. Lomascolo to the FMM construction.

References

[1] Schmitz, T. and Smith, K.S., 2012, Mechanical Vibrations: Modeling and Measurement, Springer, New York, NY, 2012.
[2] Ewins, D.J., 1984, Modal Testing: Theory and Practice, Vol. 15, Research Studies Press, Letchworth.
[3] Lomascolo, C., Ziegert, J., and Schmitz, T., 2016, Displacement-based measurement of static and dynamic coefficients of friction, American Society for Precision Engineering Annual Meeting, October 23-28, Portland, OR.
[4] Kossack, C., Schmitz, T., and Ziegert, J., 2017, Identification of friction energy dissipation using free vibration velocity: Measurement and modeling, American Society for Precision Engineering Annual Meeting, October 29-November 3, Charlotte, NC.
[5] Inman, D.J., 2008, Engineering Vibration, Vol. 3, Prentice Hall, New Jersey.
[6] Kalpakjian, S. and Schmid, S., 2008, Manufacturing Processes for Engineering Materials, 5th Ed., Prentice Hall, Upper Saddle River, NJ.
[7] Astakhov, V., 2006, Tribology of Metal Cutting, Elsevier Science and Technology, Oxford, UK.
[8] Astakhov, V., 1998, Metal Cutting Mechanics, CRC Press, Boca Raton, FL.
[9] Tlusty, G., 1999, Manufacturing Processes and Equipment, Prentice Hall, Upper Saddle River, NJ.
[10] Yang, X. and Liu, C.R., 2002, A new stress-based model of friction behavior in machining and its significant impact on residual stresses computed by finite element method, International Journal of Mechanical Sciences, 44: 703-723.
[11] Olsson, H., Åström, K.J., Canudas de Wit, C., Gäfvert, M., and Lischinsky, P., 1998, Friction models and friction compensation, European Journal of Control, 4/3: 176-195.
[12] Armstrong-Helouvry, B., 1991, Control of Machines with Friction, Boston, MA, Kluwer.
[13] Armstrong-Helouvry, B., Dupont, P., and Canudas de Wit, C., 1994, A survey of models, analysis tools and compensation methods for the control of machines with friction, Automatica, 30/7: 1083-1138.
[14] Berger, E.J., 2002, Friction modeling for dynamic system simulation, Applied Mechanics Reviews, 55/6: 535-577.
[15] Hsu, S, Ying, C., and Fei Z., 2014, The nature of friction: A critical assessment, Friction, 2/1: 1-26.
[16] Barahanov, N. and Ortega, R. , 2000, Necessary and sufficient conditions for passivity of the LuGre friction model, IEEE Transactions on Automatic Control, 45/4: 830-832.
[17] Bliman, P.A. and Sorine, M., 1995, Easy-to-use realistic dry friction models for automatic control, Proceedings of the 3rd European Control Conference, ECC'95, Rome, Italy, pp. 3788-3794.
[18] Canudas de Wit, C., Olsson, H., Astrom, K.J., and Lischinsky, P., 1995, A new model for control of systems with friction, IEEE Transactions Automatic Control, 40: 419-425.
[19] Dahl, P., 1968, A solid friction model, The Aerospace Corporation, El Segundo, CA, Tech. Rep. TOR-0158(3107-18).
[20] Dupont, P., Hayward, V., Armstrong, B., and Altpeter, F., 2002, Single state elastoplastic friction models, IEEE Transactions Automatic Control, 47: 683-687.
[21] Ferretti, G., Magnani, G., Martucci, G., Rocco, P., and Stampacchia, V., 2003, Friction model validation in sliding and presliding regimes with high resolution encoders, Experimental Robotics VIII, B. Siciliano and P. Dario, Eds. New York: Springer-Verlag, pp. 328-337.
[22] Ferretti, G., Magnani, G., and Rocco, P., 2004, Single and multistate integral friction models, IEEE Transactions Automatic Control, 49: 2292-2297.
[23] Lampaert, V., Swevers, J., and Al-Bender, F., 2002, Modification of the Leuven integrated friction model structure, IEEE Transactions on Automatic Control, 47/4: 683-687.

[24] Swevers, J., Al-Bender, F., Ganseman, C.G., and Prajogo, T., 2000, An integrated friction model structure with improved presliding behavior for accurate friction compensation, IEEE Transactions Automatic Control, 45: 675-686.
[25] Lampaert, V., Al-Bender, F., and Swevers, J., 2003, A generalized Maxwell-slip friction model appropriate for control purposes, IEEE International Conference on Physics and Control Proceedings-PhysCon, St. Petersburg, Russia, pp. 24-31.
[26] Makkar, C., Dixon, W., Sawyer, W.G., and Hu, G., 2005, A new continuously differentiable friction model for control systems design, Proceedings of the 2005 IEEE/ASME International Conference on Advanced Intelligent Mechatronics, Monterey, CA, July 24-28, pp. 600-605.
[27] Jamaludin, Z., Brussel, H. V., Pipeleers, G., and Swevers, J, 2008, Accurate motion control of XY high-speed linear drives using friction model feedforward and cutting forces estimation, CIRP Annals – Manufacturing Technology, 57/1: 403-406.
[28] Schmitz, T., Action, J., Ziegert, J., and Sawyer, W.G., 2005, The difficulty of measuring low friction: Uncertainty analysis for friction coefficient measurements, Journal of Tribology, 127: 673-678.
[29] Liang, J.W. and Feeny, B., 1998, Identifying Coulomb and viscous friction from free-vibration decrements, Nonlinear Dynamics, 16: 337-347.